





## The Peruvian oxygen minimum zone was similar in extent but weaker during the Last Glacial Maximum than Late Holocene

Nicolaas Glock <sup>1</sup>, Zeynep Erdem <sup>2</sup> & Joachim Schönfeld<sup>3</sup>

Quantifying past oxygen concentrations in oceans is crucial to improving understanding of current global ocean deoxygenation. Here, we use a record of pore density of the epibenthic foraminifer *Planulina limbata* from the Peruvian Oxygen Minimum Zone to reconstruct oxygen concentrations in bottom waters from the Last Glacial Maximum to the Late Holocene at 17.5°S about 500 meters below the sea surface. We found that oxygen levels were 40% lower during the Last Glacial Maximum than during the Late Holocene (about 6.7 versus 11.1  $\mu\text{mol}/\text{kg}$ , respectively). A comparison with other reconstructions of oxygen concentrations in the region reveals a shallow Oxygen Minimum Zone during the Last Glacial Maximum that was similar in water depth and extent but weaker than during the Late Holocene. Increased glacial oxygen concentrations are probably related to lower temperatures (higher oxygen solubility), decreased nutrient and increased oxygen supply by source waters, and a decrease in coastal upwelling.

<sup>1</sup>Institute for Geology, University of Hamburg, Bundesstraße 55, 20146 Hamburg, Germany. <sup>2</sup>NIOZ Royal Netherlands Institute for Sea Research, PO Box 59, 1790 AB Den Burg, The Netherlands. <sup>3</sup>GEOMAR Helmholtz Centre for Ocean Research Kiel, Wischhofstrasse 1-3, 24148 Kiel, Germany. email: [nicolaas.glock@uni-hamburg.de](mailto:nicolaas.glock@uni-hamburg.de)

Ongoing ocean deoxygenation and the expansion of tropical oxygen minimum zones (OMZs) due to a combination of climate warming and anthropogenic fertilization became a challenging task for contemporary earth science<sup>1,2</sup>. The Peruvian OMZ in the Eastern Tropical South Pacific is one of the most distinctive regions of oxygen (O<sub>2</sub>) depletion in the oceans and biogeochemical cycling within this region influences global biogeochemistry. In particular, OMZs are major regions of reactive nitrogen (N) loss by denitrification or anammox<sup>3</sup> and have a strong impact on global carbon cycling, since photosynthetic organisms bind atmospheric CO<sub>2</sub> near the water surface and fixed carbon is transported into the deep via downward flux of organic matter<sup>4</sup>. Vice versa dissolved CO<sub>2</sub> from deeper water masses is released to the atmosphere via upwelling<sup>4</sup>. The cold, upwelled deeper water masses warm up when they are transported to the water surface, which reduces the CO<sub>2</sub>-solubility. Bioproductivity in these regions therefore has substantial influence on the atmospheric CO<sub>2</sub> concentrations. The hydrography at the Peruvian margin is dominated by the O<sub>2</sub> rich, equatorward Peru-Chile Current (flowing in depths between 0–100 m) and the O<sub>2</sub> deficient, nutrient-rich, poleward Peru-Chile undercurrent (flowing between ~100–350 m)<sup>5–10</sup>. The Chile-Peru Deep Coastal Current prevails at ~500 m water depth near the coast and transports fresh and cold Antarctic Intermediate Water northwards<sup>11</sup>. Depending on the latitude this current competes with the Peru-Chile undercurrent that is dominant ~500 m between 16°S and 17°S<sup>11</sup>. At greater depths, the Antarctic Intermediate Water competes with North Pacific Intermediate Water, which results in different mixing flavors around Eastern Equatorial North and South Pacific<sup>12</sup>. Coastal upwelling off Peru is perennial and wind-driven<sup>8,13</sup>.

A quantitative assessment of pre-anthropogenic Peruvian OMZ extension and OMZ fluctuations between cold (glacial) and warm (interglacial) periods is still missing. There are only a few approaches of quantitative deglacial O<sub>2</sub> reconstructions at the Peruvian OMZ so far, which are based on the variation of benthic foraminifera assemblages and redox sensitive elements in the sediments<sup>14,15</sup>. These studies indicated a decrease in bottom water O<sub>2</sub> concentrations ([O<sub>2</sub>]<sub>BW</sub>) of ~30 μmol/kg in intermediate depths (~1000–1250 m) of the northern OMZ boundary<sup>14</sup> and a loss of 5–10 μmol/kg O<sub>2</sub> at 240 m in the OMZ center at 11°S<sup>15</sup> between the Last Glacial Maximum (LGM) and the Late Holocene (LH). This is equal to a loss of about 50% O<sub>2</sub> in intermediate water depths. The results are supported by other semi-quantitative redox proxies, such as the ratio of redox sensitive elements in the sediments (i.e., Mo/Re) and the variability of stable N-isotopes in sedimentary organic matter (δ<sup>15</sup>N<sub>org</sub>), both indicating O<sub>2</sub> depletion over the last deglaciation<sup>16</sup>.

The porosity of epibenthic *Cibicides* spp. is an emerging foraminifera based quantitative O<sub>2</sub> proxy that has recently been calibrated<sup>17</sup>. Some deep dwelling planktic foraminifera also adapt their porosity to O<sub>2</sub> variability<sup>18</sup>. Pore size and shape are conservative morphological features in evolution and species-specific<sup>19–21</sup>. In addition, the factors that influence the porosity of benthic foraminifera also appear to vary between different species. Epifaunal *Cibicides* spp. seem to require O<sub>2</sub> for aerobic respiration, since they increase their porosity under O<sub>2</sub> depletion to optimize the uptake of O<sub>2</sub><sup>17</sup>. Some denitrifying foraminifera such as *Bolivina spissa* adapt their pore density (PD = pores/surface-area) to the availability of nitrate (NO<sub>3</sub><sup>-</sup>) instead of O<sub>2</sub> and can be used as quantitative proxy for bottom water NO<sub>3</sub><sup>-</sup> concentration ([NO<sub>3</sub><sup>-</sup>]<sub>BW</sub>)<sup>22,23</sup>. Several species of benthic foraminifera are able to denitrify when O<sub>2</sub> is to be depleted for respiration<sup>24–28</sup>. *B. spissa* belongs to a group of

denitrifying species that prefer NO<sub>3</sub><sup>-</sup> over O<sub>2</sub> as an electron acceptor<sup>29</sup>. It is possible that some *Cibicides* spp. can switch to denitrification under O<sub>2</sub> depletion, since they cluster next to the known denitrifying species within the phylogenetic tree<sup>30</sup>. It has been assumed for a while that *Cibicidoides wuellerstorfi* cannot survive longer O<sub>2</sub> depletion<sup>31</sup>. However, Rathburn et al.<sup>17</sup> observed living *Cibicidoides* spp. in environments of <2 μmol/kg [O<sub>2</sub>]. In addition, fossil specimens have been found in paleorecords during periods of severe O<sub>2</sub> depletion<sup>32</sup>. Though, *Cibicidoides* spp. usually seem to prefer O<sub>2</sub> respiration, since living specimens can be found in [O<sub>2</sub>] of up to 275 μmol/kg<sup>17</sup> even if some might be able to denitrify during periods of O<sub>2</sub> depletion.

In this study we test if the PD of the epibenthic foraminifer *Planulina limbata* from the Peruvian OMZ might also be used as a quantitative O<sub>2</sub> proxy by comparing four different methods for PD determination. We show, that the PD of *P. limbata* from core tops of five short sediment cores from the Peruvian OMZ is significantly correlated to [O<sub>2</sub>]<sub>BW</sub>. Finally, we use our new local and species-specific calibration to quantify the [O<sub>2</sub>]<sub>BW</sub> change between the LGM and the LH using sediment cores from the southern boundary of the Peruvian OMZ (17.5°S) and compile our record with other quantitative records from this region to assess the change in OMZ extension and strength between the LGM and the LH.

## Results

**Core stratigraphy.** The age models of cores M77/1 416-GC4 and M77/1 406-MUC6 (locations see Fig. 1 and Table 1) are mainly based on radiocarbon dating. In addition, the δ<sup>18</sup>O record has been used to exclude some samples from M77/1 406-MUC6 that were obviously located below a hiatus. None of the samples contained a sufficient number of planktic foraminifera for radiocarbon dating. Thus, the age model for core M77/1 416-GC4 is completely based on radiocarbon ages of epibenthic *P. limbata* (Table 2). There is an offset in radiocarbon ages between benthic and planktic foraminifera, based on the ventilation age of the bottom water and the marine reservoir age (MRA) of the surface water, in which planktic foraminifera are dwelling (see review by Skinner and Bard<sup>33</sup>). To minimize this age uncertainty, we used the benthic-planktic radiocarbon age offset of the closest sediment core in literature that provided this data for our time slice of interest, which is CDH 26 (03°59.160S, 81°18.520W, 1023m)<sup>12</sup>. Since the location of CDH 26 is ~500 m deeper than M77/1 416-GC4, we assume that the ventilation age was likely a bit higher at CDH 26 resulting in a slight overestimation of our benthic-planktic offset. After the benthic-planktic radiocarbon age offset correction we did an additional MRA correction, using the MRA values for 18.75°S 75°W for the different time slices from the model output by Butzin et al.<sup>34,35</sup> (Supplementary Fig. 1). The radiocarbon ages of core M77/1 406-MUC6 that were measured on sedimentary organic matter were only MRA corrected using the model output by Butzin et al.<sup>34,35</sup> (Supplementary Fig. 1). The corrected radiocarbon dates were calibrated using Intcal20<sup>36</sup>. Age-depth models (Fig. 2) and sedimentation rates (Supplementary Fig. 2) for both cores were calculated, using the Bchron software package<sup>37</sup>. One outlier in core M77/1 416-GC4 that showed an age reversal at 290 cm depth was excluded for construction of the age depth model. The calibrated ages and all the correction steps are summarized in Table 2.

Both cores showed a distinct hiatus. The longer core M77/1 416-GC4 only covered the LGM from 17.5 to 24.1 cal. kyr BP. The Deglaciation and Holocene are missing. Benthic δ<sup>18</sup>O were relatively uniform along M77/1 416-GC4 and showed an offset of

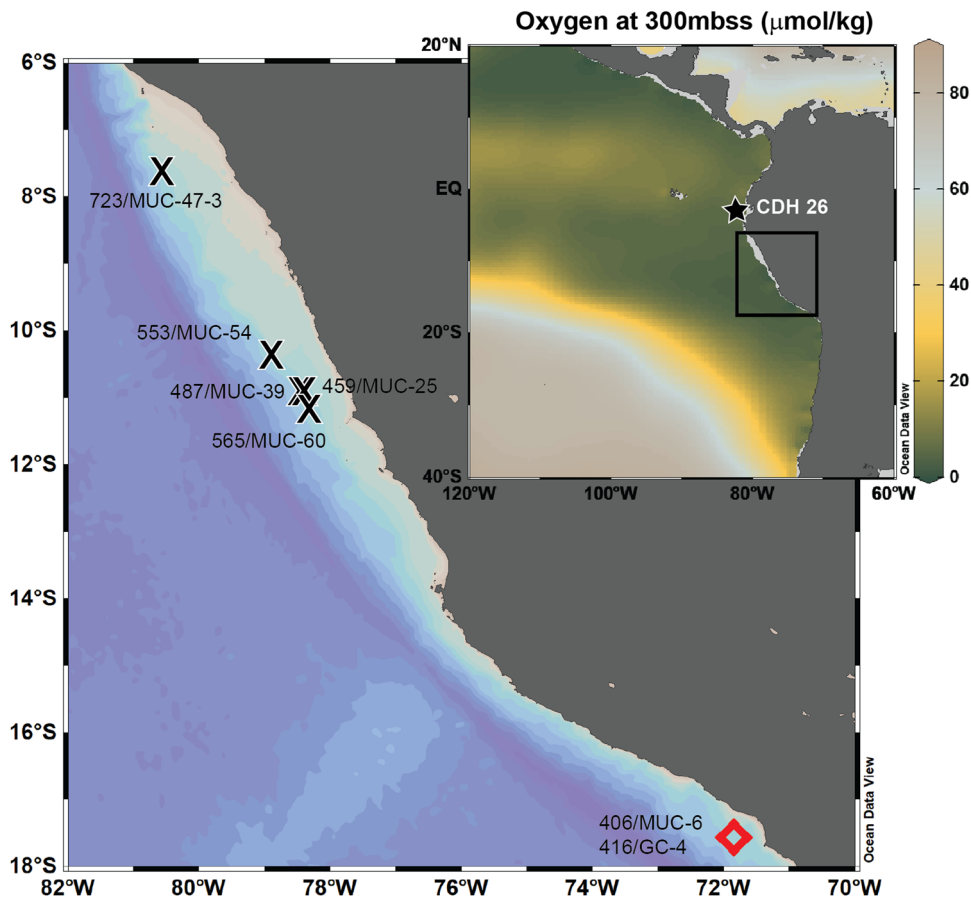


**Fig. 1 Map of sampling locations.** Map with sampling locations together with dissolved oxygen concentration at 300 mbss in the Southeastern Pacific Ocean (inset map). Data are obtained from World Ocean Atlas 2018<sup>59</sup>. Black crosses indicate the locations of MUC samples used for the core top calibration of PD vs.  $[O_2]_{BW}$ . Red diamond shows the location of sediment cores M77/1-406/MUC-6 and M77/1-416/GC-4 used for the paleoreconstruction of  $[O_2]_{BW}$ . Prepared using Ocean Data View<sup>65</sup>. The black star in the inlet map shows the location of CDH 26 that has been used for the benthic planktic offset correction of our radiocarbon data (taken from Bova et al.<sup>12</sup>).

**Table 1 Station list.**

Station	Latitude (°W)	Longitude (°S)	Water depth (m)	$[O_2]_{BW}$ (μmol/kg)
M77/1-553/MUC-54	78°54.70'	10°26.38'	521	3.00 <sup>a</sup>
M77/1-487/MUC-39	78°23.17'	11°00.00'	579	3.70 <sup>b</sup>
M77/2-723/MUC-47-3	80°31.36'	07°52.01'	626	8.10 <sup>a</sup>
M77/1-565/MUC-60	78°21.40'	11°08.00'	640	8.17 <sup>b</sup>
M77/1-459/MUC-25	78°25.60'	11°00.02'	698	12.55 <sup>b</sup>
M77/1-406/MUC-6	71°52.40'	17°28.00'	492	c
M77/1-416/GC-4	71°52.62'	17°28.14'	505	c

Stations for the calibration and stations that have been used for the paleo  $O_2$  reconstructions are divided by a line. Station names in italic letters indicate that these stations were used for the paleo  $O_2$  reconstruction. The other stations were used for the modern PD calibrations.

<sup>a</sup> $[O_2]_{BW}$  taken from Glock et al.<sup>66</sup>.

<sup>b</sup> $[O_2]_{BW}$  taken from Glock et al.<sup>22</sup>.

<sup>c</sup>The  $[O_2]$  gradient at the lower OMZ boundary was very steep at this location which results in a highly variable modern  $[O_2]_{BW}$ . Different data sources list values between 1 and 25 μmol/kg<sup>57-60</sup>.

around ~1‰ compared to the top centimeters of M77/1 406-MUC6. One ‰ is a common offset between LGM and LH (see Supplementary Fig. 3). In core M77/1 406-MUC6 benthic  $\delta^{18}O$  shows an abrupt step to glacial values below 10 cm sediment depth in addition to a jump in the radiocarbon age in this part of the core (Table 2). Since these depths were obviously located below a hiatus, we ignored the PD data from this part of the core, since these foraminifera were not from the LH. We also excluded the elevated radiocarbon age of sedimentary organic matter at ~14 cm depth for the construction of our age-depth model. Only the first 10 cm of M77/1 406-MUC6 were used for our paleo

reconstructions, since they were from the LH. The sedimentation rates were much lower during the LH in comparison to the LGM (Supplementary Fig. 2). Both the hiatus and the low sedimentation rates during the LH are a typical phenomenon for this region in similar water depths. A widespread hiatus evolved in this region over the last deglaciation, likely due to erosion through high energetic non-linear internal waves<sup>38</sup>. Under modern conditions low sedimentation rates are common in water depths ~500 m at the Peruvian Margin because the internal waves hit the seafloor in these depths within a critical angle, which facilitates erosion<sup>39</sup>.

**Table 2 Radiocarbon (<sup>14</sup>C) dating results for cores M77/1 416-GC4 and M77/1 406-MUC6.**

Core name	Depth (cm)	Type	<sup>14</sup> C age (14C year)	SD	Benthic-planktic offset (14C year) <sup>12</sup>	Benthic SD from Benthic-planktic offset (14C year) <sup>12</sup>	Planktic SD from Benthic-planktic offset (14C year) <sup>12</sup>	Benthic-planktic corrected 14C age (14C year)	MRA (14C year) <sup>35</sup>	Propagated SD	Cal. age min (year BP)	Cal. age max (year BP)
M77/1 416-GC4	20	<i>P. limbata</i>	15,900	60	850	60	65	15,050	782	107	17,087	17,788
M77/1 416-GC4	60	<i>P. limbata</i>	16,910	70	850	60	65	16,060	832	113	18,275	18,759
M77/1 416-GC4	100	<i>P. limbata</i>	17,690	80	1000	70	70	16,690	904	127	18,842	19,402
M77/1 416-GC4	110	<i>P. limbata</i>	17,560	80	1000	70	70	16,560	888	127	18,747	19,283
M77/1 416-GC4	160	<i>P. limbata</i>	18,080	90	1000	70	70	17,080	925	134	19,146	19,855
M77/1 416-GC4	210	<i>P. limbata</i>	18,610	80	1250	100	70	17,360	978	146	19,447	20,172
M77/1 416-GC4	230	<i>P. limbata</i>	18,970	80	1250	100	70	17,720	1045	146	19,682	20,481
M77/1 416-GC4	245	<i>P. limbata</i>	19,370	90	850	90	110	18,520	1094	168	20,610	21,664
M77/1 416-GC4	250	<i>P. limbata</i>	19,550	100	850	90	110	18,700	1058	174	20,905	21,919
M77/1 416-GC4	290	<i>P. limbata</i>	18,930	90	850	90	110	18,080	1133	168	20,040	20,853
M77/1 416-GC4	310	<i>P. limbata</i>	21,050	130	850	90	110	20,200	994	193	22,669	23,716
M77/1 416-GC4	345	<i>P. limbata</i>	22,560	120	1400	160	80	21,160	964	215	23,838	23,838
406-MUC6	0-2	Bulk C <sub>org</sub>	800	30				148	652	30	9	275
MUC6	5-8	Bulk C <sub>org</sub>	1500	30				848	652	30	690	882
MUC6	14-18	Bulk C <sub>org</sub>	8070	40				7379	691	40	8043	8320

<sup>14</sup>C ages were determined on epibenthic *Planulina limbata* in M77/1 416-GC4 and on bulk sedimentary organic matter (Bulk C<sub>org</sub>) for core M77/1 406-MUC6. All <sup>14</sup>C ages have been corrected for the marine reservoir ages (MRA) for 18.75°S 75°W for the different time slices modeled by Butzin et al.<sup>34,35</sup> (Supplementary Fig. 1). <sup>14</sup>C ages of *P. limbata* were additionally corrected for the benthic-planktic <sup>14</sup>C offset measured in CDH 26 by Bova et al.<sup>12</sup>. SDs are the standard deviations. Propagated SDs for M77/1 416-GC4 include the errors from *P. limbata* in this core and the planktic and benthic <sup>14</sup>C ages from Bova et al.<sup>12</sup>. The range (2.5–97.5%) of the calibrated ages (Cal. age) has been modeled from the corrected atmospheric (atm.) <sup>14</sup>C age with Intcal20<sup>36</sup> using the Bchron software package<sup>37</sup>. Data in italic letters has been excluded from the age model, due to age reversals/redeposition (see text for details).

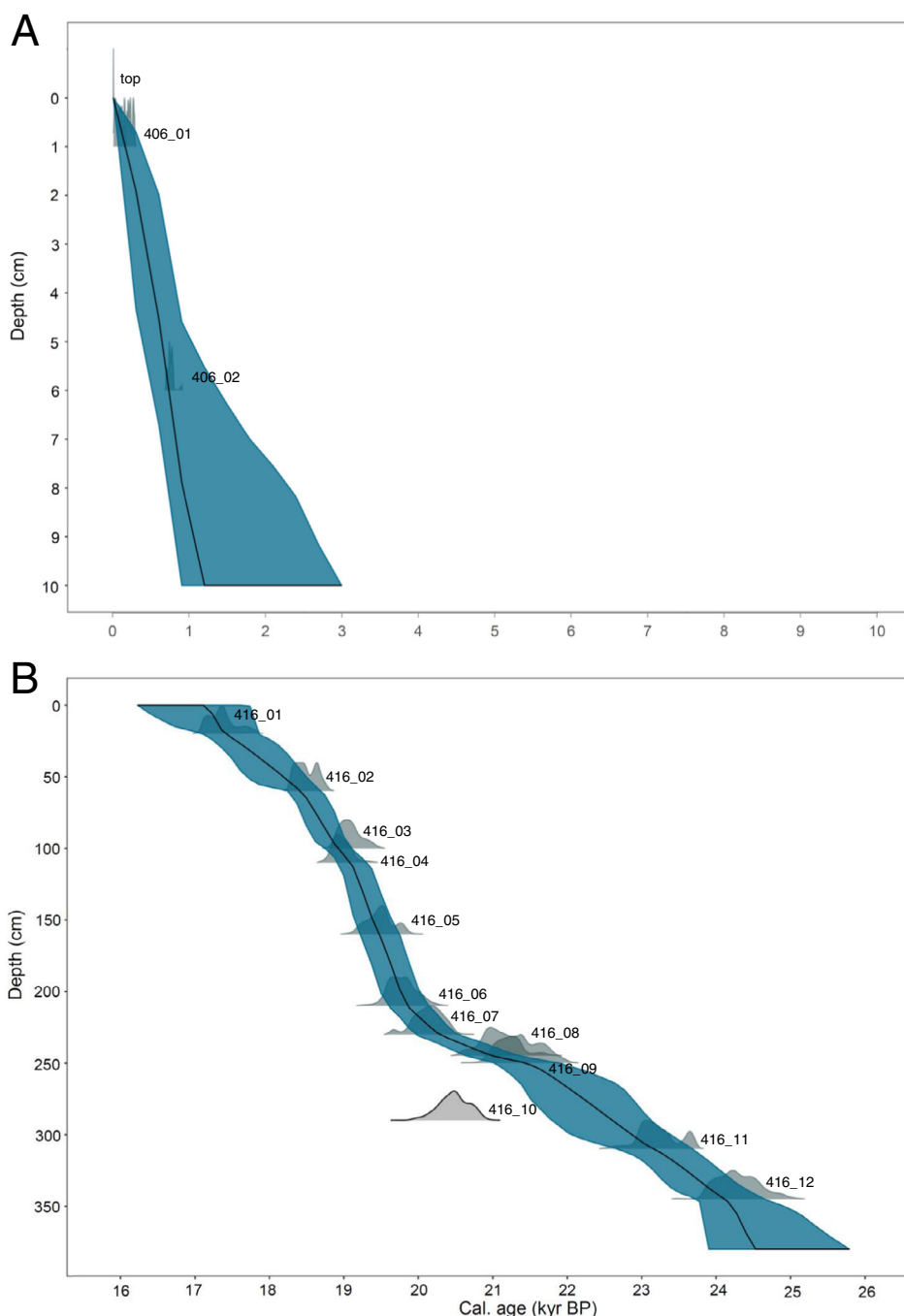


**Fig. 2** Age-depth models for sediment cores M77/1 406-MUC6 and M77/1 416-GC4. Age-depth models for cores M77/1 406-MUC6 (**A**) and M77/1 416-GC4 (**B**). These models are based on  $^{14}\text{C}$  dating and have been modeled using the Bchron software package<sup>37</sup>. Error bands show 95% confidence intervals. The probability distributions and highest density regions are shown for the  $^{14}\text{C}$  age of each analyzed sample. Note that sample 416\_10 has been excluded from the age model as an outlier (age reversal).

### Comparison of four different methods to determine foraminiferal pore density

**A: Description of the tested methods.** Four different methods were applied and tested to determine the PD of *P. limbata* in order to compare the data with the global porosity calibration on *Cibicides* spp. from Rathburn et al.<sup>17</sup> and to achieve the best possible local calibration of PD vs.  $[\text{O}_2]_{\text{BW}}$  (see also Fig. 3).

#1.: According to Rathburn et al.<sup>17</sup> and Petersen et al.<sup>40</sup> PDs from the core top samples were determined in the middle of the chamber within a rectangular window with a size of  $\sim 5000 \mu\text{m}^2$ . This method has the advantage that a very smooth and flat

surface can be chosen and artifacts by the curvature of the sample are avoided. Rathburn et al.<sup>17</sup> analyzed the ultimate and penultimate chambers. We always chose the best preserved chamber without cracks or overgrowths that was closest to the ultimate chamber. This was in most cases either the ultimate or penultimate chamber (Fig. 3A).

#2.: PDs were determined on the umbilical side of the whole specimen. Pores were counted manual and the PD is the average of the whole specimen<sup>41</sup> (Fig. 3B).

#3.: Same as method #2 but the spiral side was used instead of the umbilical side<sup>41</sup> (Fig. 3C).

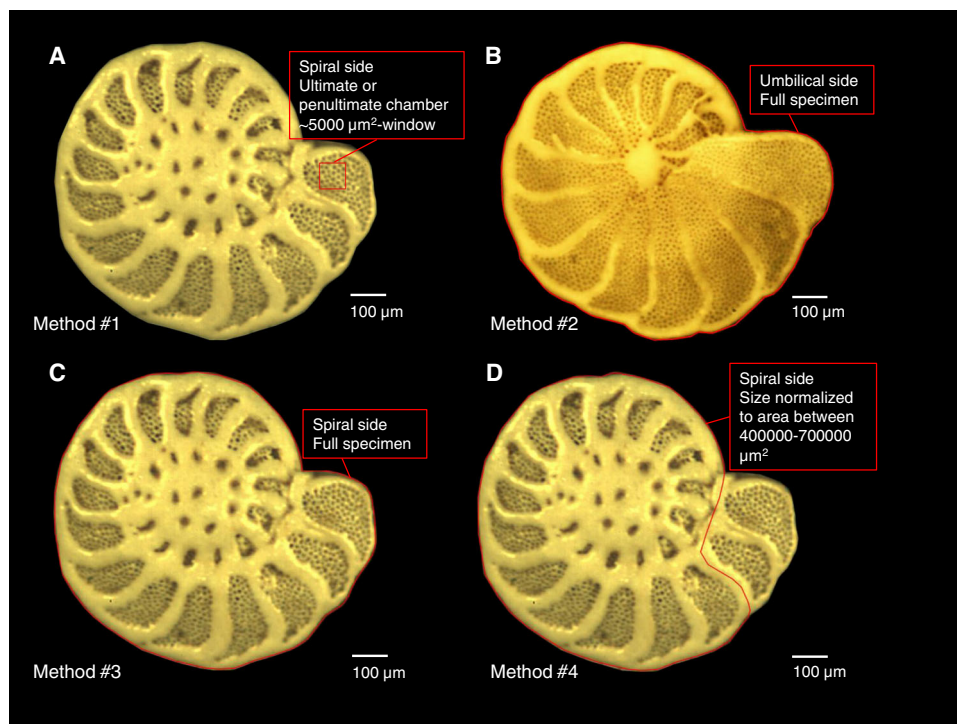


**Fig. 3 Visual descriptions of pore density (PD) determination methods.** Visual description of the four methods that have been compared to determine the PD of *Planulina limbata*. For a detailed description of these methods see text. **A** Method #1; **B** Method #2; **C** Method #3; **D** Method #4.

#4.: Same as method #3 but the samples were size normalized to minimize ontogenetic effects<sup>41</sup>. Specimens that had a smaller surface area than  $400,000 \mu\text{m}^2$  were excluded from the dataset and for specimens larger than  $700,000 \mu\text{m}^2$  the last number of chambers were excluded until the total analyzed area was  $<700,000 \mu\text{m}^2$  (Fig. 3D).

**B: Statistical comparison of the tested methods.** For comparison, the four methods have been applied to determine the PD of *P. limbata* in the core top samples (locations see Fig. 1 and Table 1; results see Table 3 for averages and Supplementary Data 1 for all individual PDs). The core top PDs of *P. limbata* that have been determined with method #1 were compared with the epifaunal PDs by Rathburn et al.<sup>17</sup> (Fig. 4A). Our new data complemented the dataset by Rathburn et al.<sup>17</sup> since it mainly added datapoints within the lower  $[\text{O}_2]_{\text{BW}}$  range. Logarithmic regression through the compiled datasets showed a highly significant relationship between the PD of epibenthic foraminifera with  $[\text{O}_2]_{\text{BW}}$  ( $R^2 = 0.80$ ;  $F = 572$ ;  $p < 0.0001$ ) over a wide range from saturated  $\text{O}_2$  to nearly anoxic conditions ( $[\text{O}_2] < 2 \mu\text{mol/kg}$ ). The PD is higher at locations with lower  $[\text{O}_2]$  (visual example at Fig. 4B).

All of the four tested PD determination methods showed a significant relationship between the mean core top PD of *P. limbata* and  $[\text{O}_2]_{\text{BW}}$  at the five locations that were used for our local calibration (Fig. 4C–F). Method #1 showed the worst correlation ( $R^2 = 0.92$ ;  $F = 33$ ;  $p = 0.01$ ) while the correlation was best using method #4 ( $R^2 = 0.97$ ;  $F = 86$ ;  $p = 0.0026$ ). We therefore decided to use method #4 for our downcore  $[\text{O}_2]_{\text{BW}}$  reconstruction in M77/1 416-GC4 and M77/1 406-MUC6. Only for one downcore datapoint we used method #3, since the specimens were too small for the size normalization (see Table 4).

**Downcore  $[\text{O}_2]_{\text{BW}}$  reconstruction using the pore density epifaunal *P. limbata*.** The  $[\text{O}_2]_{\text{BW}}$  for two time slices (LGM  $\sim 20$ – $17$  kyr BP and LH  $\sim 1$ – $0$  kyr BP) were reconstructed at the southern boundary of the Peruvian OMZ ( $\sim 17.5^\circ\text{S}$ ;  $\sim 500$  mbss)

using the PD of epifaunal *P. limbata* (Fig. 5 and Table 4 and Supplementary Data 2 for all individual PDs). The short core M77/1-406/MUC-6 was used for the LH slice, while the longer M77/1-416/GC-4 was used for the LGM slice. As mentioned above, only the data above 10 cm depth was used for core M77/1-406/MUC-6 due to the hiatus below 10 cm depth. The specimens at a depth of 3.5 cm were very small and out of the range for the size normalization in method #4. For 3.5 cm depth we used the calibration of method #3 to calculate  $[\text{O}_2]_{\text{BW}}$ . Due to the low number of specimens in the depths 5.5 cm, 7 cm and 9 cm, we decided to pool the specimens to one datapoint in Fig. 5. The average depth (7.6 cm) was used to calculate the age of this datapoint.

The PD was significantly higher for the LH in comparison to the LGM ( $p < 0.001$ ;  $N = 114$ ; Welch's *t*-test), indicating distinct deoxygenation at the southern boundary of the Peruvian OMZ after the LGM. The mean  $[\text{O}_2]_{\text{BW}}$  was  $11.1 \mu\text{mol/kg}$  during the LGM and  $6.7 \mu\text{mol/kg}$  during the LH indicating a loss of  $\sim 40\%$   $\text{O}_2$  at this location between these two time slices. The  $[\text{O}_2]_{\text{BW}}$  was relatively constant during the LGM and, with one exception, always higher than during the LH. Only at  $\sim 18.7$  kyr BP, a sudden drop of  $[\text{O}_2]_{\text{BW}}$  was recognized.

## Discussion

**Modern pore density calibration for epibenthic foraminifera and methodological recommendations.** Our new data for the correlation of the PD of the epibenthic species *P. limbata* to  $[\text{O}_2]_{\text{BW}}$  very well match the dataset for *Cibicides* spp. of Rathburn et al.<sup>17</sup> (Fig. 4A). Both datasets shown in Fig. 4A used method #1 for the PD determination. Rathburn et al.<sup>17</sup> suggested to use the porosity instead of the PD for  $[\text{O}_2]$  reconstruction, since they found a better correlation for the porosity. This is a good option for high resolution scanning electron micrographs but our study is based on light micrographs that do not have a resolution allowing to accurately determine the pore area. Thus, we focused on the PD instead. This has the advantage that paleoreconstructions can solely be

**Table 3 Mean pore densities (PD), standard deviations (SD) and standard errors of the mean (SEM) for the core top samples that have been used for the modern calibrations.**

Station	Mean PD after Method #1 (P/μm <sup>2</sup> )	SD	SEM	Mean PD after Method #2 (P/μm <sup>2</sup> )	SD	SEM	Mean PD after Method #3 (P/μm <sup>2</sup> )	SD	SEM	Mean PD after Method #4 (P/μm <sup>2</sup> )	SD	SEM
M77/1-459/ MUC-25	0.0049	0.00210	0.00148	0.0023	0.00051	0.00036	0.0016	0.00012	0.00009	0.0016	0.00012	0.00009
M77/1-487/ MUC-39	0.0064	0.00042	0.00013	0.0055	0.00064	0.00019	0.0031	0.00030	0.00009	0.0030	0.00030	0.00009
M77/1-553/ MUC-54	0.0062	0.00085	0.00025	0.0053	0.00045	0.00013	0.0031	0.00045	0.00013	0.0031	0.00052	0.00015
M77/1-565/ MUC-60	0.0053	0.00045	0.00013	0.0033	0.00045	0.00014	0.0021	0.00029	0.00009	0.0021	0.00029	0.00009
M77/2-723/ MUC-47-3	0.0053	0.00060	0.00018	0.0043	0.00061	0.00018	0.0025	0.00037	0.00011	0.0025	0.00042	0.00013

Data includes all the four different methods that have been tested to determine foraminiferal PDs.

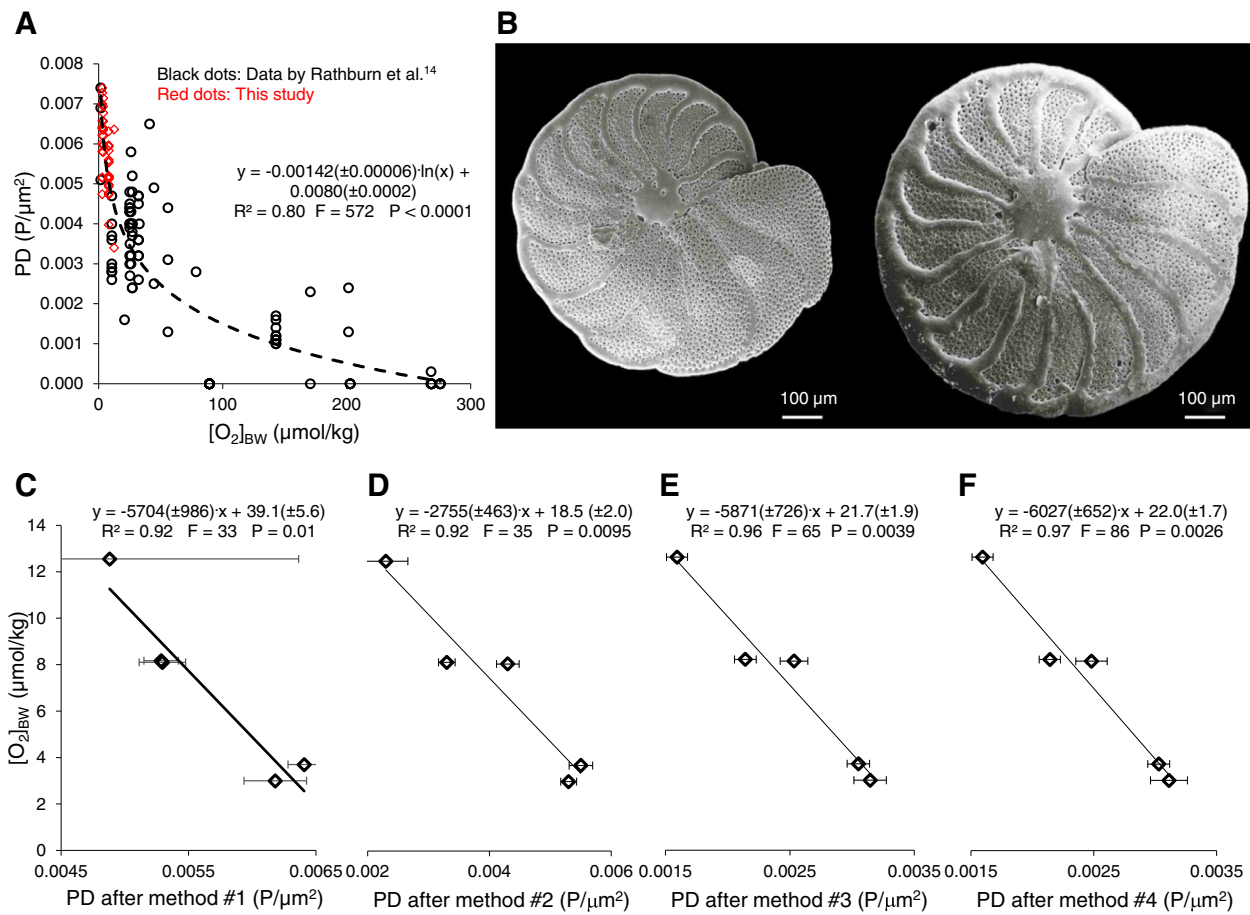


**Fig. 4 Comparison of results and calibrations for different pore density (PD) determination methods.** **A** Comparison of epifaunal PD vs. bottom water  $O_2$  concentrations ( $[O_2]_{BW}$ ) correlation between our study (*Planulina limbata*; red dots) and Rathburn et al.<sup>17</sup> (Mixed species; black dots). PDs of each individual foraminiferal specimen are plotted. All PDs in this plot were determined after method #1. The dashed line is a logarithmic regression through all datapoints (Equation and statistics are shown in figure). **B** Scanning electron micrographs of two epifaunal *P. limbata* specimens (umbilical side) with different porosity features. Left specimen (higher porosity) is from M77/1-487/MUC-39 ( $[O_2]_{BW} = 3.70 \mu\text{mol/kg}$ ); Right specimen (Lower porosity) is from M77/1-565/MUC-60 ( $[O_2]_{BW} = 8.17 \mu\text{mol/kg}$ ). **C–F** Comparison of the four methods that have been tested to determine the correlation between  $[O_2]_{BW}$  and the mean the PD of *P. limbata* in each sample. For a detailed description of these methods see text. **C** Method #1; **D** Method #2; **E** Method #3; **F** Method #4. Solid lines are linear regressions (Equation and statistics are shown in figure). Error bars are the standard error of the mean (1 SEM).

based on optical images that only need a stereo microscope or a macro objective with a good magnification coupled to a digital (optical) camera, which is less expensive and time consuming than electron microscopy.

Our data for *P. limbata* from the Peruvian OMZ is in good agreement with the data for *Cibicides wuellerstorfi*, *Cibicides lobatulus* and *Planulina* sp. from the global dataset by Rathburn et al.<sup>17</sup>. This indicates that all these species adapt their PD in a similar way to  $O_2$  availability and it is likely that the correlation can be adapted to other epibenthic species from a wide range of habitats as well. It has to be emphasized that this is different for denitrifying foraminifera such as *B. spissa*, which adapts its PD to  $[NO_3^-]_{BW}$ <sup>22,23</sup>. We cannot exclude, though, that *P. limbata* as well as some other *Planulina* and *Cibicides* spp. might be able to switch to denitrification under severe  $O_2$  depletion. Several *Cibicides* spp. cluster in the phylogenetic tree close to the known foraminiferal denitrifiers<sup>30</sup>.

In literature there are different methods suggested for the determination of pore characteristics of benthic foraminifera. The most common method is to focus on a small window within a smooth surface in the middle of the ultimate or penultimate chamber<sup>17,19,20,40,42,43</sup> (Method #1 in this study). This has several advantages. This type of analysis is relatively fast, it minimizes

artifacts related to the curvature of the specimens, normalizes regarding the ontogenetic stage of the specimen and negates problems with overgrown pores. Nevertheless, the dataset for each individual foraminifer is limited, due to the small window size that is usually used for this method and there might be another factor that influences the pore characteristics in the ultimate and penultimate chambers: the stability of the test. Porosity and PD usually increases from the oldest to the youngest chamber related to the decreasing surface to volume ratio with increasing size of the specimen<sup>22</sup>. Our results also showed that the PD determined after method #1 was generally higher in comparison to the other methods (Fig. 4C–F). Other recent studies described that the stability of the foraminiferal test is decreasing with increasing porosity<sup>43</sup>. Richirt et al.<sup>43</sup> also found that different *Ammonia* phenotypes increase their porosity by building less but larger pores in their ultimate or penultimate chamber since the walls have more stability this way instead of simply building more pores. This might not be the case in older, less porous parts of the test where the porosity is not high enough to restrict the stability of the test walls. Finally, Method #1 ignores the pore free area between and on the outside corners of the test walls. These areas increase with increasing  $[O_2]_{BW}$  (Fig. 4B).



**Table 4 Mean pore densities (PD) of *P. limbata*, calibrated ages (Cal. age) from the age model and reconstructed bottom water O<sub>2</sub> concentrations ([O<sub>2</sub>]<sub>BW</sub>) for the downcore reconstructions in cores M77/1 406-MUC6 and M77/1 416-GC4.**

Core name	Depth (cm)	Cal. age (year BP)	SD	PD (P/μm <sup>2</sup> )	SD	SEM	[O <sub>2</sub> ] <sub>BW</sub> (μmol/kg)	SEM
M77/1 406-MUC6	0.5	86	42	0.0027	0.00024	0.00011	5.7	1.3
M77/1 406-MUC6	1.5	252	90	0.0027	0.00013	0.00005	6.0	1.0
M77/1 406-MUC6	2.5	361	100	0.0024	0.00038	0.00019	7.5	1.6
M77/1 406-MUC6	3.5	461	102	0.0029	0.00024	0.00014	4.8	1.8
M77/1 406-MUC6	4.5	559	96	0.0026	*	*	6.3	2.4(SD)
M77/1 406-MUC6	4.5	559	96	0.0023	*	*	8.3	2.2(SD)
M77/1 406-MUC6	7.6	1010	291	0.0022	0.00019	0.00010	8.5	1.2
M77/1 416-GC4	20.0	17,432	203	0.0017	0.00022	0.00009	11.5	1.0
M77/1 416-GC4	30.0	17,721	209	0.0016	0.00024	0.00011	12.1	1.1
M77/1 416-GC4	40.0	17,943	196	0.0016	0.00011	0.00005	12.6	0.8
M77/1 416-GC4	50.0	18,165	179	0.0017	0.00018	0.00008	11.8	1.0
M77/1 416-GC4	55.0	18,288	161	0.0019	0.00034	0.00015	10.3	1.3
M77/1 416-GC4	65.0	18,524	124	0.0017	0.00026	0.00012	11.7	1.1
M77/1 416-GC4	70.0	18,582	120	0.0016	0.00012	0.00006	12.2	1.0
M77/1 416-GC4	75.0	18,636	116	0.0015	0.00020	0.00010	13.0	1.1
M77/1 416-GC4	85.0	18,737	108	0.0024	0.00029	0.00013	7.6	1.3
M77/1 416-GC4	90.0	18,792	103	0.0017	0.00030	0.00014	11.5	1.2
M77/1 416-GC4	100.0	18,922	85	0.0016	0.00016	0.00007	12.1	1.0
M77/1 416-GC4	110.0	19,105	104	0.0018	0.00012	0.00005	11.3	1.0
M77/1 416-GC4	120.0	19,191	107	0.0019	0.00025	0.00012	10.5	1.3
M77/1 416-GC4	135.0	19,286	114	0.0019	0.00014	0.00006	10.7	1.0
M77/1 416-GC4	140.0	19,318	117	0.0020	0.00021	0.00009	10.1	1.1
M77/1 416-GC4	150.0	19,383	123	0.0020	0.00031	0.00014	10.2	1.2
M77/1 416-GC4	160.0	19,467	132	0.0019	0.00027	0.00012	10.8	1.2
M77/1 416-GC4	180.0	19,625	129	0.0020	0.00043	0.00019	10.2	1.5

All PDs were determined after method #4, except in the one sample in italic letters. In this sample specimens were too small for size normalization and PD and [O<sub>2</sub>]<sub>BW</sub> were determined using method #3. Only two specimens were found in 4.5 cm depth. PDs and reconstructed [O<sub>2</sub>]<sub>BW</sub> are listed here for each individual instead as mean values for the whole sample. SD standard deviation, SEM standard error of the mean. An asterisk symbol "\*" indicates that this is the PD from a single specimen and no SD or SEM could be calculated for this sample.

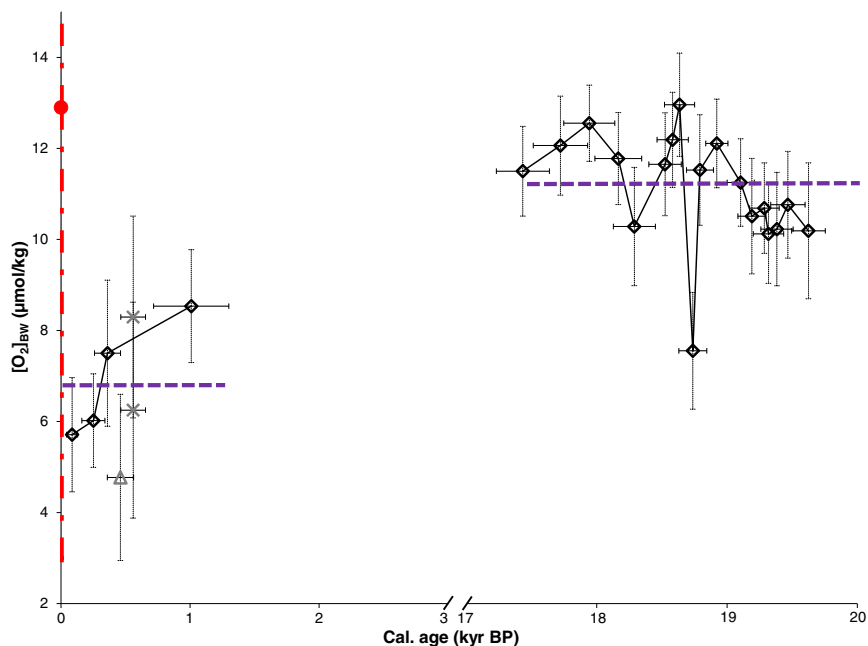


**Fig. 5 Paleorecord of bottom water O<sub>2</sub> concentrations ([O<sub>2</sub>]<sub>BW</sub>) at the Southern Peruvian OMZ.** Quantitative palaeorecord of mean [O<sub>2</sub>]<sub>BW</sub> in cores M77/1 406-MUC6 and M77/1 416-GC4 using the PD of *Planulina limbata*. The X-axis is broken at 3 kyr BP. Note that the slice during the Late Holocene (LH) is from M77/1 406-MUC6 and the slice from the Last Glacial Maximum (LGM) from core M77/1 416-GC4. All PDs were determined after method #4, except in the one sample plotted as a gray triangle. In this sample specimens were too small for size normalization and PD and [O<sub>2</sub>]<sub>BW</sub> were determined using method #3. Since only two specimens were found in one sample each individual reconstructed [O<sub>2</sub>]<sub>BW</sub> instead of mean values were plotted as gray crosses. (4.5 cm depth) Horizontal errors are the standard deviation (1 SD) Vertical error bars are standard error of the mean (1 SEM) except for the gray crosses (1 SD). Mean modern [O<sub>2</sub>]<sub>BW</sub> in this region is highly variable in this region (range from 1–25 μmol/kg<sup>57–60</sup>). The red dot represents the mean modern [O<sub>2</sub>]<sub>BW</sub> (red dashed line = 1 SD). Note that all the reconstructed [O<sub>2</sub>]<sub>BW</sub> are within the range of short time modern variability.

Another method, that has been used for PD determination, is to focus on a larger size normalized part of the older chambers of the foraminifer<sup>22,23</sup> (Method #4 in this study). This method has the advantages that the ontogenetic effects are also minimized by size normalization and the larger area provides a larger dataset for each individual and the stability of the test walls is less restricting, since the older parts of the test are usually less porous. The main disadvantages of this method is the higher effort that is necessary to acquire the data, the problem that pores in older chambers might be overgrown and artifacts by the curvature of the tests.

An additional method that recently came up is the automated image analysis to determine the porosity on shards of benthic foraminifera after crushing using optical microscopy<sup>44</sup>. From all the methods so far this appears to be the least time consuming and it is possible to generate huge datasets with relatively low effort. Though, this method is destructive and it is not possible to archive the specimens. Also the use of the specimens for other analyses might be limited. Finally, a method has been suggested for automated morphometric analysis on benthic foraminifera using atomic force microscopy<sup>45</sup>. This approach most likely generates the most metadata, since it is even possible to measure the depth and 3D shape of the pores but it is also the most effortful of the methods discussed above.

Our methodological comparison also tested if it is better to use the umbilical (Method #2) or the spiral side (Method #3 and 4) of the foraminifer for the PD analysis (Fig. 4D–F). The correlation between the PD of *P. limbata* and  $[O_2]_{BW}$  was better using the spiral side. The average umbilical PD is much higher than the average spiral PD. The closely related *Planulina ariminensis* was found on stalked substrates well above the sediment surface in that spiral and umbilical sides were exposed in the same way to the bottom-near water<sup>46</sup>. Therefore, the worse correlation on the umbilical side might be related to stability restrictions of the test wall due to the elevated porosity<sup>43</sup>. In addition, due to the higher PD, the determination on the umbilical side is usually more effortful. We thus suggest to focus on the spiral side of the specimens for the application of PD or porosity as a paleo proxy. Since we found the best correlation between PD and  $[O_2]_{BW}$  using method #4 for our local calibration, we also used this method for our paleo  $[O_2]_{BW}$  reconstructions in this region. This does not mean that this is the best approach for other regions and foraminiferal species. The dataset using method #1 is now relatively large including the global data by Rathburn et al.<sup>17</sup> and our new data for *P. limbata* for the Peruvian OMZ. For  $[O_2]$  reconstructions in regions of larger  $[O_2]$  variability where no local calibration is available, we would therefore recommend to use method #1 and the correlation shown in Fig. 4A. Though, our dataset includes only specimens from  $O_2$  depleted locations. If  $[O_2]$  should be reconstructed at locations with higher  $O_2$  levels it might be good to focus on the calibration by Rathburn et al.<sup>17</sup> and porosity instead of the PD might be used if high resolution electron micrographs are available.

**Deoxygenation off Peru between the Last Glacial Maximum and the Late Holocene.** Our  $[O_2]_{BW}$  paleo reconstruction at 17.5°S off Peru (~500 mbss) indicates a deoxygenation from ~11.1 to 6.7  $\mu\text{mol/kg}$ , which is equal to an  $O_2$  loss of ~40% (~5  $\mu\text{mol/kg}$ ). This is in good agreement with other quantitative  $[O_2]$  reconstructions in this region. Scholz et al.<sup>15</sup> found an  $[O_2]$  drop of 5–10  $\mu\text{mol/kg}$  at 11°S (240 mbss) and Erdem et al.<sup>14</sup> an  $[O_2]_{BW}$  decrease of ~50% in intermediate water depths (~1000–1250 mbss) below the Peruvian OMZ between the LGM and the LH. The modern  $O_2$  in the Peruvian OMZ is located in water depths between 300 and 400 mbss<sup>16</sup>. With ~500 m water depth sites M77/1 406-MUC6 and M77/1-416/GC-4 are located at the lower

OMZ boundary. During the LGM, the sea level was ~120 m lower<sup>47</sup>. Thus, sites M77/1 406-MUC6 and M77/1-416/GC-4 would be shifted into water depths of today's core OMZ. This indicates that  $[O_2]_{BW}$  during the LGM was higher even within the core OMZ than compared to the lower OMZ boundary during the LH.

The elevated  $[O_2]_{BW}$  during the LGM is in good agreement with trends in several data compilations for the Pacific Ocean<sup>48,49</sup>. The simultaneous increase of  $[O_2]$  during the LGM in all parts of the Peruvian OMZ is likely caused by interactions between decreased temperatures, higher  $[O_2]$  to the subsurface water masses, the supply of preformed nutrients to the subtropics and decreased coastal upwelling off Peru. The low sea surface temperatures during the LGM resulted in an increase of  $O_2$  solubility and a generally higher  $[O_2]$  in and increased formation of intermediate water masses, that supply  $O_2$  to subsurface water masses off Peru<sup>15,16,50</sup>. In addition, there was likely increased Fe supply to higher latitudes during the LGM, related to the lower sea level, due to the decrease in shelf sediments and increased erosion<sup>51,52</sup>. This Fe fertilization at high latitudes stimulated primary productivity at the Southern Ocean which resulted in increased burial of preformed nutrients to the deep Southern Ocean<sup>23,52</sup>. This reduced the concentration preformed nutrients in Subantarctic Mode Water, which supplied nutrients to the subtropics, and affected limitation of primary productivity at lower latitudes<sup>23,52</sup>. Less  $O_2$  was consumed by remineralization below the photic zone due to this decrease in primary productivity. This is supported by a quantitative  $NO_3^-$  record at the Northern part of the Peruvian OMZ<sup>23</sup>. Finally, the intertropical convergence zone experienced a southward shift during the LGM at the Eastern Tropical Pacific, implying a general decrease in coastal upwelling in this region<sup>16,53</sup>. A study on the change in nutrient utilization at the Peruvian OMZ during the last deglaciation based on stable Si isotope fractionation also infers a decrease in upwelling during the LGM at 15°S close to our study site<sup>54</sup>. Though, due to the distinct hiatus at our location there is only a slight overlap in this record and our data at the end of the LGM.

The common observation that  $[O_2]$  at the Peruvian OMZ was higher during the LGM in shallow depths ~240 m<sup>15</sup>, intermediate depths ~500 m (this study) and “deep”-intermediate depths ~1000–1250 m<sup>14</sup> indicates that the LGM conditions at the Eastern Tropical South Pacific were decoupled from the Eastern Equatorial Pacific<sup>32,55</sup>. Actually, the OMZ at the Eastern Tropical Pacific was expanded downwards during the LGM, likely due to a decrease in ventilation and an increase in the respired deep carbon storage in intermediate to deep water depths during the LGM<sup>32</sup>. In addition, a recent study showed that there was no shallow OMZ at the Eastern Equatorial Pacific during the LGM but a massive suboxygenated connecting the old  $O_2$  depleted deep to intermediate water masses<sup>55</sup>. The shallow OMZ at the Eastern Equatorial Pacific only established during the Holocene<sup>55</sup>. Our results from the regionally adjacent Peruvian margin indicate that there was a shallow OMZ at the Eastern Tropical South Pacific which was similar but less  $O_2$  depleted than during the LH (Fig. 6). We found no evidence for a severe vertical shift of the Peruvian OMZ over the last deglaciation which might have connected intermediate to deep reservoirs of old carbon to the atmosphere as it has been observed for the Eastern Equatorial Pacific<sup>55</sup>. Nevertheless, a comparison of the available quantitative  $[O_2]$  paleo data with modern conditions indicates that the oxycline below the OMZ is steeper today than during the LGM or the LH. This might indicate that the intermediate to deep water masses at the Peruvian Margin have been ventilated very recently. The  $[O_2]_{BW}$  below 800 mbss are based on foraminiferal assemblages<sup>14</sup>. In the original study it is discussed that the

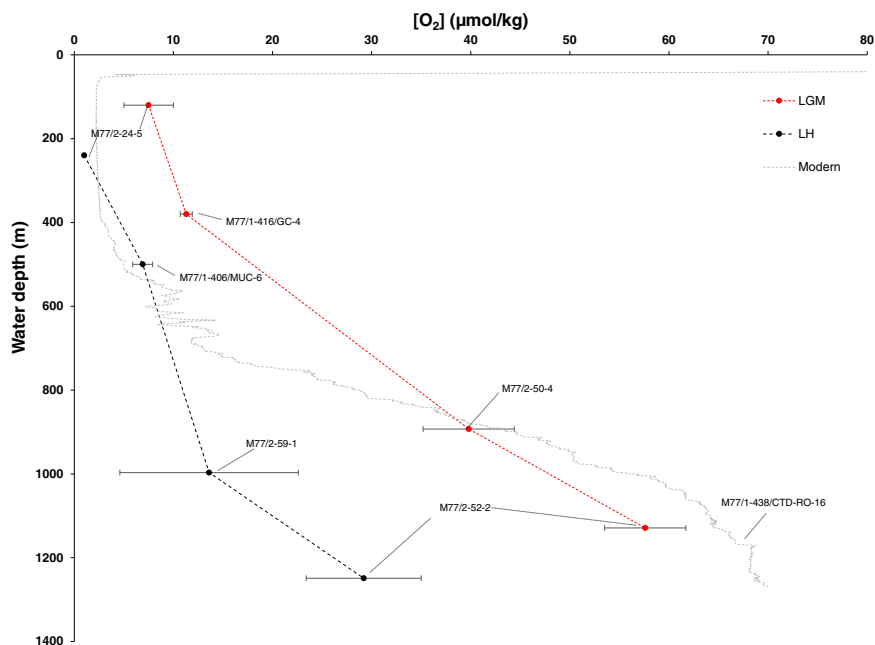


**Fig. 6 Comparison of the Peruvian OMZ during the LGM, the LH and modern conditions.** Bottom water  $O_2$  concentrations ( $[O_2]_{BW}$ ) reconstructed with different approaches for different depths at the Peruvian OMZ during the LGM (red) and the LH (Black). Data at 1000–1250 m are from Erdem et al.<sup>14</sup>, at ~500 m from this study and ~240 m from Scholz et al.<sup>15</sup>. Modern data are from 11°S M77/1-438/CTD-RO-16<sup>57</sup>. Note that water depths during the LGM have all been corrected by the lower sea level of ~120 m<sup>47</sup>. Datapoints for our data and Erdem et al.<sup>14</sup> are the weighted mean for each time slice and error bars are the standard error for the weighted mean. Scholz et al.<sup>15</sup> indicated a range of 5–10  $\mu\text{mol/kg}$  for the LGM (shown here as  $7.5 \pm 2.5 \mu\text{mol/kg}$ ). The data for the LH from Scholz et al.<sup>15</sup> were calculated after their Fig. 1b and indicated always anoxic conditions (here shown as 1  $\mu\text{mol/kg}$  without error bar).

reconstructed  $[O_2]_{BW}$  might be biased to lower values, because the majority of reference surface samples used for the calibration were from shallower locations (e.g., lower  $[O_2]_{BW}$  than the stations, used for the paleoreconstructions). Thus, we cannot exclude that the flattened lower oxycline during the LH might be an artifact, related to results of multiple  $[O_2]$  paleo proxies being compiled in Fig. 6.

During the LGM time slice there are no obvious trends in  $[O_2]_{BW}$  at site M77/1-416/GC-4 indicating that the conditions were relatively stable during this time interval. The LH time slice at site M77/1 406-MUC6 starts ~1 kyr BP. Within this time interval there is a distinct trend in decreasing  $[O_2]_{BW}$  over time. A record of sea surface temperatures ~17°S, close to our location documented a strong cooling trend during this time interval<sup>56</sup> and another record at 14°S showed an increase in sedimentary fish scales and the redox sensitive Mo/Re ratio<sup>16</sup>. Thus, the decreasing bottom water  $[O_2]_{BW}$  over the past 1 kyr are likely related to an increase in upwelling and primary productivity in this region. Mean modern  $[O_2]_{BW}$  close to our study site is highly variable (range from ~1–25  $\mu\text{mol/kg}$ <sup>57–60</sup>). All the  $[O_2]_{BW}$  in our palaeorecord are within this range of modern  $[O_2]_{BW}$  variability (see Fig. 5). Though, there seem to be  $[O_2]$  pulses ~17.5°S at ~500 m that exceed our averaged values from the palaeorecord. This might be related to seasonality in the life cycle of *P. limbata*. If the reproduction of *P. limbata* is coupled to the main upwelling season, the PD likely records the lower  $[O_2]_{BW}$  during that season. It also might be possible that foraminifera adapt their pore density to the lowest seasonal  $[O_2]$  they experience. The higher  $O_2$  pulses would not matter in that case, since the foraminifera are already adapted to withstand even lower  $[O_2]$ . The lowest modern  $[O_2]_{BW}$ , documented close to the coring sites (M77/1-416/GC-4 and M77/1 406-MUC6) was ~1  $\mu\text{mol/kg}$ , which is below the range of reconstructed  $[O_2]_{BW}$  using the PD proxy. This might indicate that the seasonally lowest  $[O_2]_{BW}$  continued to decrease during the LH. A recent study offered an

alternative hypothesis: Belanger<sup>61</sup> found that the adult morphology of benthic foraminifera might already be predetermined by the environmental conditions that the individual experiences during the embryonic state<sup>61</sup>. If this applies to the foraminiferal PD as well, it would corroborate that *P. limbata*'s life cycle is coupled to the main upwelling season and that the PD is consequently adapted to lower  $[O_2]_{BW}$  than the annual mean. Another explanation for the fact that the highly variable modern  $[O_2]_{BW}$  sometimes exceeds the range of our paleorecord could be an observation that bottom waters at the Peruvian shelf became more oxygenated over the last ~100 years<sup>62</sup>.

The observation that the Peruvian OMZ was more oxygenated during the LGM in comparison to the Holocene and modern conditions (Fig. 6) is in line with recent observations of on-going ocean deoxygenation and OMZ expansion related to global warming<sup>1,2</sup>. The Peruvian OMZ is at present in a highly productive state and the abundance of anchovies actually increased over the past ~1 kyr, following the trend for other proxies for subsurface ocean deoxygenation<sup>16</sup> and our own data (Fig. 5). The optimum in anchovy production off Peru during the modern warm period is related to the enhanced nutrient supply that increases primary productivity and the related preferential development of large plankton<sup>16</sup>. Although the current warm period seems to be favorable for the Peruvian anchovy population and the related commercial fishery, some periods during the LH that are characterized by a very intense OMZ are disadvantageous for anchovy populations<sup>16</sup>. Indeed, there is evidence that smaller goby like fish species dominated the Peruvian upwelling region in a very warm and severely  $O_2$  depleted phase during the Eemian<sup>63</sup>. Ocean deoxygenation will likely continue under the current trend of global warming and indeed anchovy biomass steadily decreased again during the past decades<sup>2,63</sup>. Thus, there is a high risk that the ecosystem at the Peruvian upwelling region reaches a tipping point for the fish community. This might potentially result in jellyfish outbreaks leading to a trophic dead

end, as observed in other ecosystems where fisheries have collapsed, such as the Benguela Upwelling<sup>64</sup>. Our results indicate deoxygenation at the Peruvian OMZ from the cold LGM to the warm LH, and the current warm period and thus provide further evidence for concerns related to the foreseeable future ocean deoxygenation.

In conclusion, our quantitative  $[O_2]_{BW}$  is in good agreement with other paleorecords from the Peruvian OMZ and the combined datasets of these studies indicate a similar but weaker OMZ during the LGM. We found a deoxygenation of ~40% in intermediate water at 17.5°S off Peru between the LGM and the LH which is likely related to higher temperatures (lower  $O_2$  solubility), increased nutrient and decreased  $O_2$  supply by source waters and an increase in coastal upwelling. This is a contrasting situation to the adjacent Eastern Equatorial Pacific, which had an expansion of  $O_2$  depleted waters to deeper depth but better ventilated shallow waters during the LGM<sup>32,55</sup>.

## Methods

**Sampling procedure.** Six short sediment cores from the Peruvian OMZ were extracted during R.V. *Meteor* cruise M77/1 in October 2008 using a video guided multicorer (Fig. 1 and Table 1). Within a couple of minutes after the multicorer came on deck, one tube was chosen from the array, and brought to a laboratory with a constant room temperature of 4 °C. Supernatant water of the core was carefully removed. Then the core was gently pushed out of the multicorer tube and cut into 12 slices (10-mm-thick) for benthic foraminiferal analysis. The samples were transferred to Whirl-Pak™ plastic bags and transported at a temperature of 4 °C. One additional long sediment core (3.88 m) was extracted using a gravity corer (M77/1 416-GC4; Table 1). This core was immediately cut into one meter sections and each section was sliced into two halves (work and archive half). These were stored and transported back at a temperature of 4 °C. The samples of these seven cores were used to collect the specimens for the PD analyses, radiocarbon dating and benthic foraminiferal  $\delta^{18}O$  measurements.

**Foraminiferal studies.** The sediment samples were washed over a 63- $\mu$ m mesh sieve and dried at 50 °C. They were further subdivided into the grain-size fractions of 63–125, 125–250, 250–315, 315–355, 355–400, and >400  $\mu$ m. Specimens of the epifaunal species *P. limbata* were picked from the >400  $\mu$ m fraction. Specimens of *Uvigerina striata* and *Uvigerina peregrina* were picked from the 355–400  $\mu$ m fraction.

Images of *P. limbata* were taken using a MiniPixie MPX2051UC CCD camera (AOS Technologies™), mounted on a macro objective (1-6233 and 1-6010 by Navitar™). The programs AxioVision, Zen and ImageJ were used for the image analyses. In total 185 specimens were used for the image analyses. We used 10–12 specimens for the core top PD vs.  $[O_2]_{BW}$  calibrations except in core M77/1-459/MUC-25, where only two well preserved specimens of *P. limbata* were available. For the downcore PD record we used an average of five *P. limbata* specimens.

Two additional specimens from M77/1-487/MUC-39 ( $[O_2]_{BW} = 3.70 \mu\text{mol/kg}$ ; see Table 1) and M77/1-565/MUC-60 ( $[O_2]_{BW} = 8.17 \mu\text{mol/kg}$ ; see Table 1) were imaged with scanning electron microscopy for visual documentation of the influence of  $[O_2]_{BW}$  on the porosity of *P. limbata* (see Fig. 4B). These two specimens were mounted on aluminum stubs, sputter-coated with gold, and imaged using a CamScan-CS-44 scanning electron microscope at the Christian-Albrecht-University in Kiel.

Additional specimens of *P. limbata* from 12 sediment depths were used for the radiocarbon dating on core M77/1 416-GC4. The radiocarbon dating for three sediment depths on core M77/1 406-MUC6 has been done on sedimentary organic matter. All radiocarbon analyses were performed at Beta Analytic, Inc., Florida, USA.

Three to six individuals of *U. peregrina* and *U. striata* were used for the stable isotope measurements ( $\delta^{18}O$  and  $\delta^{13}C$ ). The tests of the foraminiferal specimens were gently crushed between two glass slides and the fragments were mixed. The measurements were performed at GEOMAR, Kiel, using a Thermo Scientific MAT253 mass spectrometer equipped with an automated CARBO Kiel IV carbonate preparation device. The isotope values were reported in permil (‰) relative to the Vienna Pee Dee Belemnite (VPDB) scale and calibrated vs. NBS 19 (National Bureau of Standards) as well as to an in-house standard (Solnhofen limestone). Long-term analytical accuracy (1-sigma) for  $\delta^{18}O$  and  $\delta^{13}C$  was <0.06‰ and <0.03‰, respectively.

**Calculation of  $[O_2]_{BW}$  for the paleoreconstructions and error estimation.** Four different methods have been tested in this study to use the PD of *P. limbata* to reconstruct past  $[O_2]_{BW}$ . A detailed description of these methods is given in the results section. Since method #4 showed the best correlation between PD and  $[O_2]_{BW}$ , we mainly used this method for the downcore reconstructions. Only for one downcore datapoint we used method #3, since the specimens were too small for the size normalization (see Table 4).  $[O_2]_{BW}$  was therefore calculated according

to Eq. (1):

$$[O_2]_{BW} = -6027(\pm 652) \cdot PD + 22.0(\pm 1.7) \quad (1)$$

A progression of uncertainty was used to calculate the errors for the reconstructed  $[O_2]_{BW}$ . Both the uncertainty of the mean PD within each sample and the uncertainties of the calibration function were included. The propagation of uncertainty has been applied to Eq. (1), resulting in:

$$\sigma_{[O_2]_{BW}} = \sqrt{\left(\frac{\delta[O_2]_{BW}}{\delta a} \cdot \sigma_a\right)^2 + \left(\frac{\delta[O_2]_{BW}}{\delta PD} \cdot \sigma_{PD}\right)^2 + \left(\frac{\delta[O_2]_{BW}}{\delta b} \cdot \sigma_b\right)^2} \quad (2)$$

where  $\sigma_x$  is the uncertainty (1sd) of the corresponding parameter  $x$  (in this case  $[O_2]_{BW}$ ,  $a$ ,  $b$  and PD),  $a$  is the slope in Eq. (1) (in this case  $-6027$ ) and  $b$  is the X-axis intercept (in this case  $22.0$ ). Application of Eq. (2) on Eq. (1) results in Eq. (3) for the calculation of  $\sigma_{[O_2]_{BW}}$ :

$$\sigma_{[O_2]_{BW}} = \sqrt{(652 \cdot PD)^2 + (-6027 \cdot \sigma_{PD})^2 + (1.7)^2} \quad (3)$$

The standard error of the mean (SEM) was then calculated according to Eq. (4):

$$SEM_{[O_2]_{BW}} = \frac{\sigma_{[O_2]_{BW}}}{\sqrt{n}} \quad (4)$$

where  $n$  is the no. of specimens analyzed in each sample.

## Data availability

All data generated or analyzed during this study are included in the tables of this published article (and its Supplementary Information files).

Received: 9 August 2022; Accepted: 17 November 2022;

Published online: 05 December 2022

## References

- Stramma, L., Johnson, G. C., Sprintall, J. & Mohrholz, V. Expanding oxygen-minimum zones in the tropical oceans. *Science* **320**, 655 LP–655658 (2008).
- Schmidtko, S., Stramma, L. & Visbeck, M. Decline in global oceanic oxygen content during the past five decades. *Nature* **542**, 335–339 (2017).
- Lam, P. et al. Revising the nitrogen cycle in the Peruvian oxygen minimum zone. *Proc. Natl. Acad. Sci. USA* **106**, 4752–4757 (2009).
- Berger, W., Smetacek, V. & Wefer, G. Ocean productivity and paleoproductivity—an overview. In *Productivity of the Ocean: Present and Past, Dahlem Workshop Reports* (eds Berger, W. H., Smetacek, V. & Wefer, G.) 1–34 (Wiley-Interscience Publ., 1989).
- Brockmann, C., Fahrback, E., Huyer, A. & Smith, R. L. The poleward undercurrent along the Peru coast: 5 to 15°S. *Deep Sea Res. A* **27**, 847–856 (1980).
- Shaffer, G., Salinas, S., Pizarro, O., Vega, A. & Hormazabal, S. Currents in the deep ocean off Chile (30°S). *Deep Sea Res. Part I Oceanogr. Res. Pap.* **42**, 425–436 (1995).
- Shaffer, G., Pizarro, O., Djurfeldt, L., Salinas, S. & Rutllant, J. Circulation and low-frequency variability near the Chilean Coast: remotely forced fluctuations during the 1991–92 El Niño. *J. Phys. Oceanogr.* **27**, 217–235 (1997).
- Böning, P. et al. Geochemistry of Peruvian near-surface sediments. *Geochim. Cosmochim. Acta* **68**, 4429–4451 (2004).
- Mackas, D. L., Strub, P., Thomas, A. & Montecino, V. Chapter 2. Eastern Ocean Boundaries Pan-Regional Overview. *The Global Coastal Ocean: Interdisciplinary Regional Studies and Syntheses*, (eds Robinson, A. R. & Brink, K. H.) 21–59 (Harvard University Press, Cambridge, MA, 2006)
- Díaz-Ochoa, J. A. et al. Fish scales in sediments from off Callao, central Peru. *Deep Sea Res. Part II Top. Stud. Oceanogr.* **56**, 1124–1135 (2009).
- Chaigneau, A. et al. Near-coastal circulation in the Northern Humboldt Current System from shipboard ADCP data. *J. Geophys. Res. Ocean.* **118**, 5251–5266 (2013).
- Bova, S. C., Herbert, T. D. & Altabet, M. A. Ventilation of northern and southern sources of aged carbon in the eastern Equatorial Pacific during the Younger Dryas rise in atmospheric CO<sub>2</sub>. *Paleoceanogr. Paleoclimatol.* **33**, 1151–1168 (2018).
- Suess, E., Kulm, L. D. & Killingly, J. S. Coastal upwelling and a history of organic-rich mudstone deposition off Peru. In *Marine petroleum source rocks* (ed Brooks, J.) Vol. 26, 181–197 (Geological Society, London, 1987).
- Erdem, Z. et al. Bottom-water deoxygenation at the Peruvian margin during the last deglaciation recorded by benthic foraminifera. *Biogeosciences* **17**, 3165–3182 (2020).
- Scholz, F., Mcmanus, J., Mix, A. C., Hensen, C. & Schneider, R. R. The impact of ocean deoxygenation on iron release from continental margin sediments. *Nat. Geosci.* **7**, 433–437 (2014).

16. Salvatucci, R. et al. Fish debris in sediments from the last 25 kyr in the Humboldt Current reveal the role of productivity and oxygen on small pelagic fishes. *Prog. Oceanogr.* **176**, 102114 (2019).
17. Rathburn, A. E., Willingham, J., Ziebis, W., Burkett, A. M. & Corliss, B. H. A New biological proxy for deep-sea paleo-oxygen: Pores of epifaunal benthic foraminifera. *Sci. Rep.* **8**, 9456 (2018).
18. Davis, C. V., Wishner, K., Renema, W. & Hull, P. M. Vertical distribution of planktic foraminifera through an oxygen minimum zone: how assemblages and test morphology reflect oxygen concentrations. *Biogeosciences* **18**, 977–992 (2021).
19. Kuhnt, T. et al. Relationship between pore density in benthic foraminifera and bottom-water oxygen content. *Deep Sea Res. Part I Oceanogr. Res. Pap.* **76**, 85–95 (2013).
20. Richirt, J. et al. Morphological distinction of three ammonia phylotypes occurring along European coasts. *J. Foraminif. Res.* **49**, 76–93 (2019).
21. Schönfeld, J., Beccari, V., Schmidt, S. & Spezzaferri, S. Biometry and taxonomy of Adriatic *Ammonia* species from Bellaria-Igea Marina (Italy). *J. Micropalaeontol.* **40**, 195–223 (2021).
22. Glock, N. et al. Environmental influences on the pore density of *Bolivina spissa* (Cushman). *J. Foraminif. Res.* **41**, 22–32 (2011).
23. Glock, N. et al. Coupling of oceanic carbon and nitrogen facilitates spatially resolved quantitative reconstruction of nitrate inventories. *Nat. Commun.* **9**, 1217 (2018).
24. Risgaard-Petersen, N. et al. Evidence for complete denitrification in a benthic foraminifer. *Nature* **443**, 93–96 (2006).
25. Piña-Ochoa, E. et al. Widespread occurrence of nitrate storage and denitrification among Foraminifera and Gromiida. *Proc. Natl. Acad. Sci. USA* **107**, 1148–1153 (2010).
26. Woehle, C. et al. A Novel Eukaryotic Denitrification Pathway in Foraminifera. *Curr. Biol.* **28**, 2536–2543.e5 (2018).
27. Orsi, W. D. et al. Anaerobic metabolism of Foraminifera thriving below the seafloor. *ISME J.* **14**, 2580–2594 (2020).
28. Gomaa, F. et al. Multiple integrated metabolic strategies allow foraminiferan protists to thrive in anoxic marine sediments. *Sci. Adv.* **7**, eabf1586 (2021).
29. Glock, N. et al. Metabolic preference of nitrate over oxygen as an electron acceptor in foraminifera from the Peruvian oxygen minimum zone. *Proc. Natl. Acad. Sci. USA* **116**, 2860–2865 (2019).
30. Woehle, C. et al. Denitrification in foraminifera has an ancient origin and is complemented by associated bacteria. *Proc. Natl. Acad. Sci. USA* **119**, e2200198119 (2022).
31. Mackensen, A., Schmiedl, G., Harloff, J. & Giese, M. Deep-sea foraminifera in the South Atlantic Ocean; ecology and assemblage generation. *Micropaleontology* **41**, 342–358 (1995).
32. Hoogakker, B. A. A. et al. Glacial expansion of oxygen-depleted seawater in the eastern tropical Pacific. *Nature* **562**, 410–413 (2018).
33. Skinner, L. C. & Bard, E. Radiocarbon as a dating tool and tracer in paleoceanography. *Rev. Geophys.* **60**, e2020RG000720 (2022).
34. Butzin, M., Heaton, T. J., Köhler, P. & Lohmann, G. A short note on marine reservoir age simulations used in IntCal20. *Radiocarbon* **62**, 865–871 (2020).
35. Heaton, T. J. et al. Marine20—the marine radiocarbon age calibration curve (0–55,000 cal BP), simulated data for IntCal20. <https://doi.org/10.1594/PANGAEA.914500> (2020).
36. Reimer, P. J. et al. The IntCal20 Northern Hemisphere Radiocarbon Age Calibration Curve (0–55 cal kBP). *Radiocarbon* **62**, 725–757 (2020).
37. Haslett, J. & Parnell, A. A simple monotone process with application to radiocarbon-dated depth chronologies. *J. R. Stat. Soc. Ser. C Appl. Stat.* **57**, 399–418 (2008).
38. Erdem, Z. et al. Peruvian sediments as recorders of an evolving hiatus for the last 22 thousand years. *Quat. Sci. Rev.* **137**, 1–14 (2016).
39. Mosch, T. et al. Factors influencing the distribution of epibenthic megafauna across the Peruvian oxygen minimum zone. *Deep Sea Res. Part I Oceanogr. Res. Pap.* **68**, 123–135 (2012).
40. Petersen, J. et al. Improved methodology for measuring pore patterns in the benthic foraminiferal genus *Ammonia*. *Mar. Micropaleontol.* **128**, 1–13 (2016).
41. Jauch, S. *Kalibration der Porendichte von Planulina limbata als potentiellen Proxy für Redoxbedingungen in der Peruvianischen Sauerstoffminimumzone* (Christian-Albrechts-Universität zu Kiel, 2013).
42. Kuhnt, T. et al. Automated and manual analyses of the pore density-to-oxygen relationship in *Globobulimina turgida* (Bailey). *J. Foraminif. Res.* **44**, 5–16 (2014).
43. Richirt, J. et al. Scaling laws explain foraminiferal pore patterns. *Sci. Rep.* **9**, 9149 (2019).
44. Tetard, M., Beaufort, L. & Licari, L. A new optical method for automated pore analysis on benthic foraminifera. *Mar. Micropaleontol.* **136**, 30–36 (2017).
45. Giordano, L., Ferraro, L., Salvatore, M., Oscurato, S. L. & Maddalena, P. Morphometric analysis on benthic foraminifera through atomic force microscopy. *Mar. Micropaleontol.* **153**, 101775 (2019).
46. Lutze, G. F. & Thiel, H. Epibenthic foraminifera from elevated microhabitats; *Cibicides wuellerstorfi* and *Planulina ariminensis*. *J. Foraminif. Res.* **19**, 153–158 (1989).
47. Fairbanks, R. G. A 17,000-year glacio-eustatic sea level record: influence of glacial melting rates on the Younger Dryas event and deep-ocean circulation. *Nature* **342**, 637–642 (1989).
48. Jaccard, S. L. & Galbraith, E. D. Large climate-driven changes of oceanic oxygen concentrations during the last deglaciation. *Nat. Geosci.* **5**, 151–156 (2011).
49. Moffitt, S. E. et al. Paleoclimatographic insights on recent oxygen minimum zone expansion: lessons for modern oceanography. *PLoS ONE* **10**, e0115246 (2015).
50. Meissner, K. J., Galbraith, E. D. & Völker, C. Denitrification under glacial and interglacial conditions: a physical approach. *Paleoceanography* **20**, PA3001 (2005).
51. Albani, S. et al. Improved dust representation in the community atmosphere model. *J. Adv. Model. Earth Syst.* **6**, 541–570 (2014).
52. Somes, C. J., Schmittner, A., Muglia, J. & Oschlies, A. A three-dimensional model of the marine nitrogen cycle during the Last Glacial Maximum constrained by sedimentary isotopes. *Front. Mar. Sci.* **4**, 108 (2017).
53. Koutavas, A. & Lynch-Stieglitz, J. Variability of the Marine ITCZ over the Eastern Pacific during the Past 30,000 Years. In: *The Hadley Circulation: Present, Past and Future. Advances in Global Change Research*, (eds Diaz, H. F. Bradley, R. S.) vol 21 (Springer, Dordrecht, 2004). [https://doi.org/10.1007/978-1-4020-2944-8\\_13](https://doi.org/10.1007/978-1-4020-2944-8_13).
54. Doering, K. et al. Changes in diatom productivity and upwelling intensity off Peru since the Last Glacial Maximum: response to basin-scale atmospheric and oceanic forcing. *Paleoceanography* **31**, 1453–1473 (2016).
55. Davis, C. V. Deglacial restructuring of the Eastern equatorial Pacific oxygen minimum zone. *Commun. Earth Environ.* **3**, 145 (2022).
56. Salvatucci, R., Schneider, R. R., Blanz, T. & Mollier-Vogel, E. Deglacial to Holocene Ocean temperatures in the Humboldt current system as indicated by alkenone paleothermometry. *Geophys. Res. Lett.* **46**, 281–292 (2019).
57. Krahnmann, G. Physical oceanography during METEOR cruise M77/1. <https://doi.org/10.1594/PANGAEA.779798> (2012).
58. Krahnmann, G. Physical oceanography during METEOR cruise M77/3. *IFM-GEOMAR Leibniz-Institute of Marine Sciences, Kiel University* <https://doi.org/10.1594/PANGAEA.77255> (2012).
59. Boyer, T. P. et al. World ocean database 2018. <https://doi.org/10.7289/V5NZ85MT> (2018).
60. Farias, L., Carrasco, C. & Faúndez, J. Nitrous oxide and biogeochemical variables related to Intermediate Waters into Eastern South Pacific Ocean. Supplement to: Carrasco, Cristina; Karstensen, Johannes; Farias, Laura (2017): On the Nitrous Oxide Accumulation in Intermediate Waters of the Eastern South Pacific Ocean. *Front. Mar. Sci.* **4** <https://doi.org/10.3389/fmars.2017.00024> (2019).
61. Belanger, C. L. Volumetric analysis of benthic foraminifera: Intraspecific test size and growth patterns related to embryonic size and food resources. *Mar. Micropaleontol.* **176**, 102170 (2022).
62. Cardich, J. et al. Multidecadal changes in marine subsurface oxygenation off central Peru during the Last ca. 170 years. *Front. Mar. Sci.* **0**, 270 (2019).
63. Salvatucci, R. et al. Smaller fish species in a warm and oxygen-poor Humboldt Current system. *Science* **375**, 101–104 (2022).
64. Richardson, A. J., Bakun, A., Hays, G. C. & Gibbons, M. J. The jellyfish joyride: causes, consequences and management responses to a more gelatinous future. *Trends Ecol. Evol.* **24**, 312–322 (2009).
65. Schlitzer, R. Ocean data view. (2015).
66. Glock, N., Liebetrau, V. & Eisenhauer, A. I/Ca ratios in benthic foraminifera from the Peruvian oxygen minimum zone: analytical methodology and evaluation as a proxy for redox conditions. *Biogeosciences* **11**, 7077–7095 (2014).

## Acknowledgements

The scientific party on R/V Meteor cruise M77 is acknowledged for their general support and help with the coring operation and sampling. We thank Sabrina Jauch for her pioneering work on calibrating the pore density of *Planulina limbata* during her bachelor thesis. Tanita Wein provided additional student assistance to compare the methods for the determination of pore densities. Funding was provided by the Deutsche Forschungsgemeinschaft (DFG) through both the SFB 754 “Climate–Biogeochemistry Interactions in the Tropical Ocean” and N.G.’s Heisenberg grant GL 999/3-1. We thank Julien Richirt and two additional anonymous reviewers for providing constructive reviews and feedback that significantly improved our manuscript.

## Author contributions

All authors planned the sampling strategy and study design. N.G. did onboard sampling, analyzed and interpreted the foraminiferal pore density data and did core-writing of the manuscript. Z.E. sampled the material for the radiocarbon dating and the stable oxygen isotope stratigraphy. N.G., Z.E. and J.S. contributed to discussing the data and writing the manuscript.

## Funding

Open Access funding enabled and organized by Projekt DEAL.

**Competing interests**

The authors declare no competing interests.

**Additional information**

**Supplementary information** The online version contains supplementary material available at <https://doi.org/10.1038/s43247-022-00635-y>.

**Correspondence** and requests for materials should be addressed to Nicolaas Glock.

**Peer review information** *Communications Earth & Environment* thanks Julien Richirt and the other, anonymous, reviewer(s) for their contribution to the peer review of this work. Primary Handling Editor: Aliénor Lavergne. Peer reviewer reports are available.

**Reprints and permission information** is available at <http://www.nature.com/reprints>

**Publisher's note** Springer Nature remains neutral with regard to jurisdictional claims in published maps and institutional affiliations.



**Open Access** This article is licensed under a Creative Commons Attribution 4.0 International License, which permits use, sharing, adaptation, distribution and reproduction in any medium or format, as long as you give appropriate credit to the original author(s) and the source, provide a link to the Creative Commons license, and indicate if changes were made. The images or other third party material in this article are included in the article's Creative Commons license, unless indicated otherwise in a credit line to the material. If material is not included in the article's Creative Commons license and your intended use is not permitted by statutory regulation or exceeds the permitted use, you will need to obtain permission directly from the copyright holder. To view a copy of this license, visit <http://creativecommons.org/licenses/by/4.0/>.

© The Author(s) 2022